Title

Raytracing the long trace profiler

ISBN

978-1-5106-3790-0

Authors

Takacs, Peter Z

Lacey, Ian

Yashchuk, Valeriy V

Publication Date

2020-08-21

DOI

10.1117/12.2569751

Peer reviewed

Raytracing the Long Trace Profiler

Peter Z. Takacs[*a,b], Ian Lacey[b], and Valeriy V. Yashchuk[b]
[a]Surface Metrology Solutions, LLC, 19 South First Street, B-901, Minneapolis, MN 55401, USA
[b]Lawrence Berkeley National Laboratory, 1 Cyclotron Rd., Berkeley, CA 94720, USA

ABSTRACT

The optical design of the Long Trace Profiler optical system is explored with a commercial raytrace program, Zemax *OpticStudio*™ (ZOS)[1], with the intent of finding and correcting sources of systematic error. ZOS provides both geometric raytracing tools and physical optics Gaussian beam propagation and diffraction image calculation tools, and two design modes, sequential component (SC) and non-sequential component (NSC) that are optimized for different aspects of the design process. The original LTP-II system employs a singlet lens with a 1250mm focal length. It is optimized to provide minimum distortion over a surface slope angle range of ±5mrad. Using the ZOS tools, we are able to simulate ghost rays that produce distortion in the beam spot image and can minimize the distortion by deliberate misalignment of the beamsplitter (BS) components. Unfortunately, the reference beam is compromised because of the component tilts. The most recent LTP500 system design simplifies the optical system and makes the reference beam usable again, even with misalignment of the polarizing beamsplitter (PBS). Two lenses are designed for the LTP500 – a cemented doublet that has been fabricated, and a singlet with one aspheric surface. Both have focal distances of 500mm with an expanded angular measurement range of ±10mrad. The aspheric singlet provides superior performance. ZOS allows the import of wavefront measurement data produced by commercial interferometer software. We apply the wavefront error measurement from the cemented doublet to the model to show that the 19nm RMS wavefront error needs to be improved by at least a factor of ten in order to reduce the systematic error to a level that will allow the LTP to approach its design limit of a few tems of nanoradians.

Keywords: Long Trace Profiler, synchrotron radiation, calibration, metrology of x-ray optics, surface metrology, slope profilometry, optical design, raytrace

1. INTRODUCTION

The Long Trace Profiler (LTP)[2-5] belongs to a class of optical metrology instruments based on the principle of deflectometry[6, 7]. It measures surface slope based on the position of a laser beam spot at the focus of a Fourier transform lens (FTL). The LTP optical system is designed to provide a linear relationship between deflection angle and image position on the detector. The lens that does this linear angle to position conversion is commonly called an F/θ lens. It is the critical component in the LTP optical system and needs to be carefully designed to operate over a specified range of field angles with minimum distortion.

The original LTP-I was designed in the 1980's with pencil and paper before the advent of modern computer raytrace design codes.[3] It is based on the pencil beam interferometer (PBI) design of von Bieren[8, 9]. It has proved to be an invaluable tool in the improvement of x-ray mirror manufacturing technology over the ensuing years. When the original instrument was designed, mirrors that had slope errors less than 5μrad were considered state-of-the art. Now synchrotron light sources are producing fully coherent x-ray beams that demand surface slope errors in the nanoradian range. This evolution has required that the performance of the LTP be improved to keep up with the stringent requirements of x-ray beamline optics. The Advanced Light Source (ALS) Upgrade (ALS-U) project[10] has provided for the opportunity to investigate error sources in the LTP with modern optical design codes and design a system that will meet the challenges of 4th generation synchrotron optics metrology. For this work we use Zemax *OpticStudio*™ (ZOS)[1] as the design code.

2. LTP SYSTEM DESIGNS

The LTP system has undergone changes over the years as metrology requirements for x-ray mirrors have become more stringent.[3, 11-19] The design principles have been guided by the need to remove as much bulk glass as possible and the need to increase the angular measurement range. The original LTP-II optical design is shown in Fig. 1 and the most recent LTP500 design is shown in Fig. 2. The original LTP-II design incorporated a plano-convex singlet lens with a 1250mm focal length. This provided sufficient resolution with a detector having 25μm pixels designed for a field angle range of

*takaca.surfmetsoln@gmail.com; phone +1 631 833-0620

±10mrad. The LTP500 uses a cemented doublet with a focal length of 500mm designed for a field angle range of ±20mrad with 5.4µm pixels. The shorter focal length lens needs to work harder, so it has more design degrees of freedom, namely 3 spherical surfaces with 2 glass types. The most recent variant of the LTP500 design uses a singlet lens with one aspheric surface. The merits of each design will be explored in this paper.

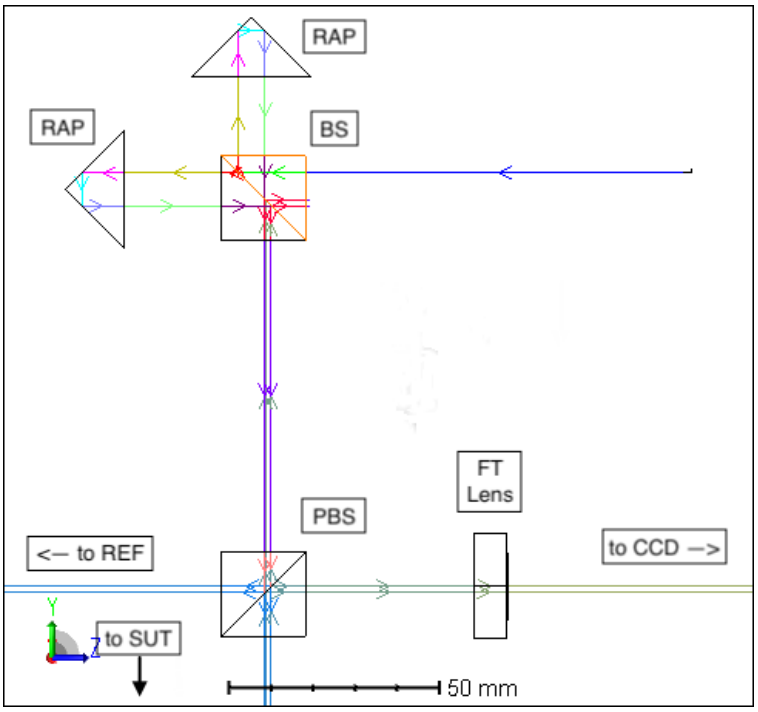

Figure 1. Basic elements of the original LTP II optical system design. Not shown are the wave plates, the folding mirrors after the lens and the polarizers after the laser to attenuate and produce a P-polarized beam. The main surface under test (SUT) and reference mirror (REF) beam rays are shown.

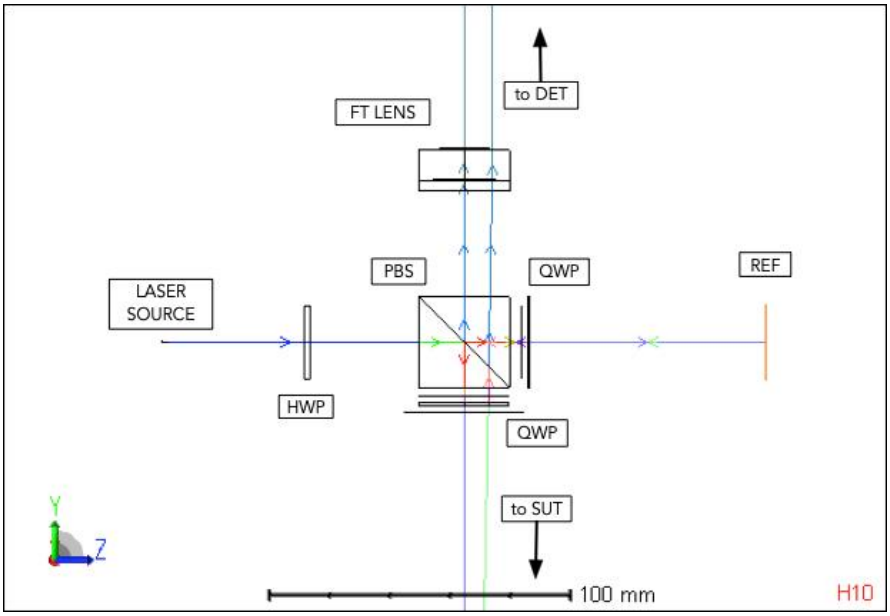

Figure 2. Basic design of most recent LTP500 implementation. Laser beam produces a single spot image with a central maximum. The FT Lens is either a cemented doublet or a singlet asphere.

3. LTP-II SYSTEM

3.1. Basic LTP-II System Components

The original LTP-II optical head design[11] is shown in Fig.1. The main design elements are the upper beamsplitter cube (BS) with right-angle prisms (RAP) that direct the laser beam back into the cube and down to the polarizing beamsplitter (PBS). One RAP is fixed; the other is mounted on a translation stage to allow for separation of the two probe beam components. The beam from the laser source is attenuated and linearly polarized before it enters the BS. There is a half-wave plate (HWP) below the BS that rotates the linear polarization so that the relative intensities between the SUT and REF beams exiting the PBS can be adjusted. This allows one to balance the intensities of the beams reflected from the reference (REF) mirror and the surface under test (SUT), which may be glass with or without a high reflectance coating. Quarter-wave plates (QWP) are placed in the REF and SUT beams after the PBS. These change the S- and P-polarized beams into left and right circularly polarized beams, which, when reflected back to the PBS, are turned into P- and S-polarized beams that are then directed into the Fourier transform lens (FTL) and on to the CCD detector (DET). The FTL has a focal length of 1250mm. The original LTP II design incorporates a set of plane folding mirrors after the FTL to fold the beam path into a more compact volume. Only the essential components necessary for the optical raytrace simulation are shown.

As in the original von Bieren PBI[8, 9], the collimated source laser beam is split into two collinear beams separated by a small distance on the order of one millimeter. With a phase difference between the beams of π, this produces an interference fringe with a central minimum at the detector. The position of the minimum is related to the local SUT slope Θ_{SUT} through the linear expression[3]

$$\Theta_{SUT} = \frac{1}{2}\frac{S_{DET}}{F}, \tag{1}$$

where S_{DET} is the fringe minimum position on the detector, F is the lens effective focal length, and the factor ½ accounts for the doubling of the SUT surface angle due to reflection. As the optical head is translated over the length of the mirror along the x-axis, the position of the fringe minimum is recorded as a function of x, and the surface slope is derived from Eq. (1) as a function of x.

One essential element in the design of the LTP is the laser beam. The original LTP-I used a HeNe laser mounted off to the side of the gantry, fixed to the granite table[3]. It was replaced by a polarized HeNe laser coupled into a long polarization-preserving single-mode fiber. This was replaced by a diode laser coupled into a single-mode fiber and eventually just a collimated diode laser mounted directly onto the optics board. The lasers were always kept on so that they would come to thermal equilibrium with their mounting structures. It is more desirable to mount the laser away from the optics board to avoid thermal drift effects altogether. The original polarization-preserving fiber was routed through the Igus cable carrier and flexed as the gantry was moved. This caused the intensity of the fiber output to fluctuate drastically, although the position of the image spot on the detector did not change at all. However, the large intensity fluctuations in the image made it difficult to keep the image intensity from saturating and distorting the fringe pattern. Fitting the minimum of the interference fringe pattern to a Gaussian function minimized the bias introduced by possible detector saturation effects. The current implementation of the ALS LTP-II[20] has the diode laser coupled to a TEM_{00} single-mode fiber with the laser separated from the temperature-sensitive optical head components. Without the polarization-preserving fiber, the intensity fluctuations are minimized. This allows for both double-beam operation with a fringe minimum or single-beam operation with a spot intensity maximum. We should note here that the spatial resolution of the LTP dramatically depends of its operation mode (two beam or one beam arrangement) and of the data processing method used for positioning of the detected interference pattern[21].

The other essential element in the design of the LTP system is the Fourier Transform lens. Figure 3 shows the relevant parameters in the lens design process. The laser beam incident on the SUT defines the aperture stop for the system. For the lens, all rays appear to originate from this aperture. A range of field angles is defined to cover the range of surface slope angles that need to be measured. For the 1250mm lens, the surface slope range is ±5mrad, so the field angle range is -10 to +10mrad. Negative field angles are not necessary due to symmetry about the optical axis. Note that the PBS thickness is an essential element in the lens design, as it introduces spherical aberration into off-axis field angles. The lens needs to compensate for this and minimize distortion. The distance between the SUT and the BS cube is an important design parameter. The lens can be optimized for a particular distance or for a range of distances. The original 1250mm lens was

designed by Jan Hoogland for a 500mm SUT-PBS distance. More recent 500mm lenses are optimized for a range of distances between 200 and 400mm.

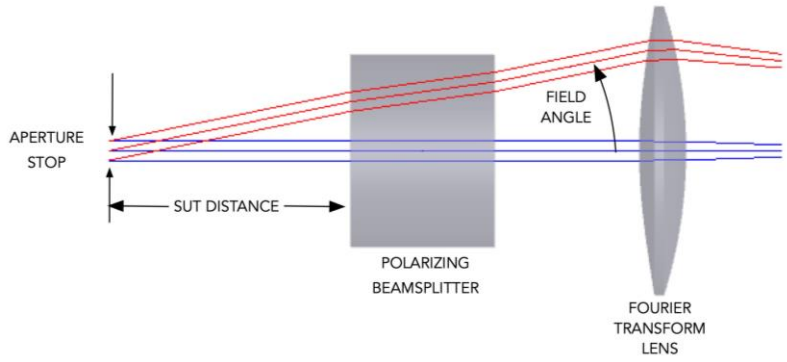

Figure 3. Relevant lens design parameters in SC mode. The laser beam reflected from the SUT appears to emanate from the aperture stop at an angle relative to the optical axis, designated as the "field angle". The thickness of the polarizing beamsplitter is essential to the lens design.

3.2. Sequential Component (SC) Raytrace Mode

ZOS has two distinct system design modes: SC and NSC. SC is the Sequential Component design mode. In this case, rays are propagated sequentially through each object as listed in the Lens Editor file. Each object is separated from the next by a thickness distance. NSC is the Non-Sequential Component design mode. Here the order of the objects in the Lens Editor is not important. Objects are placed and oriented in three-dimensional (3D) space and rays propagate to objects based on their location in space. This allows for complex off-axis system designs with ray splitting and multiple reflections. There are different analysis functions available in each mode, so it is necessary to do part of the design in one mode and then switch to the other mode to finish. The lens design is done using the SC mode. Figure 4 shows the essential components for the LTP-II lens with the 1250mm focal length. The vertical scale is stretched by a factor of 10 to make the elements more easily seen. The aperture stop on the left is located at the SUT which is 500mm in front of the cube BS. The BS is 25mm thick and the FT lens is 25mm to the right of the BS. Ray fans for the ±10mrad fields and the on-axis field are shown propagating to the detector image plane. Note that only a small part of the lens is involved at any given time in the imaging of each field. This illustrates the difference of this lens from a conventional photographic lens where the rays from each object point fill the entire lens aperture.

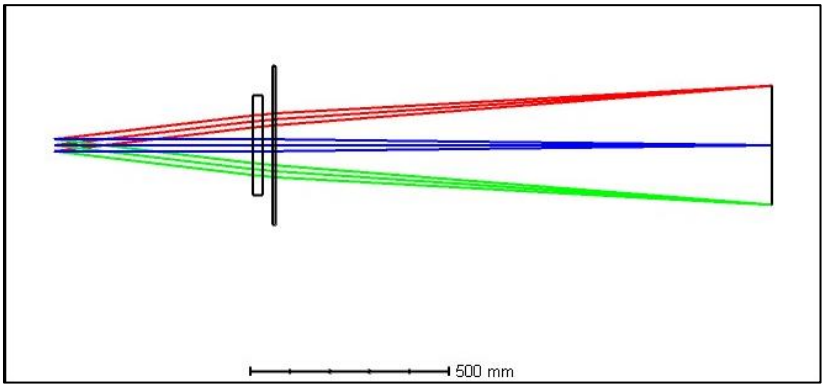

Figure 4. Objects essential to the LTP-II lens design in SC mode. Vertical scale is exaggerated by x10. The two extreme angle fields are shown, -10mrad and +10mrad, along with the on-axis 0mrad field.

ZOS has a convenient merit function optimization operand, calibrated distortion {DISC), that computes the F/θ distortion over the field angle range. For an F/θ lens, the ideal chief ray position in the focal plane is a linear function of the field

angle and the focal length: $y = F * \theta$. The DISC operand computes the maximum deviation between the real chief ray position (the ray from the center of the aperture stop along the center of the field bundle) and the expected ideal ray position. Figure 5 shows the distortion at the 500mm SUT-PBS distance as a function of field angle over the 0 to 10mrad range on the left and the maximum distortion as a function of SUT distance on the right. The Y-axis on the right is in units of millimeters with a range of 0 to 50nm. The distortion at 500mm is less than 5nm and is less than 10nm for a 100mm range about 500mm. This lens works quite well for the metrology requirements of 30 years ago. Note that the original lens was designed for a 670nm wavelength, but the changes in distortion for 633nm wavelength are insignificant.

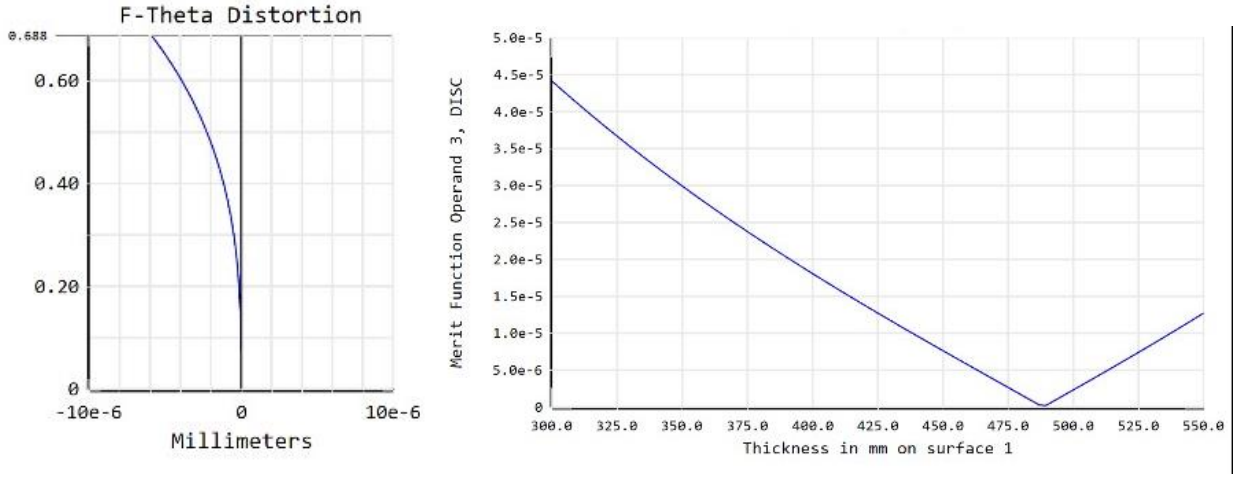

Figure 5. Distortion vs field angle for the 1250mm lens at the SUT distance of 500mm (left) , and maximum distortion as a function of SUT distance (right).

3.3. Note on coordinate system conventions

The global coordinate system in ZOS will be designated by upper case XYZ axes: +Z is oriented to the right on the page, +Y is up the page, and +X is into the page. Objects also have their own local coordinate systems. These will be designated by lower case xyz. When an object is placed into the model, its local axes initially line up with the global axes. But when an object is rotated about an axis, its local coordinate system rotates with it. In the lens editor, rotations are done relative to the local coordinate system, so one must be careful to choose the correct axis based on the rotated coordinate system. Also, the LTP gantry system has its own coordinate system. The translation axis is designated the x-axis, the vertical axis is the z-axis and the orthogonal axis in the plane of the table is the y-axis.

3.4. SC mode Physical Optics Propagator (POP)

The ZOS SC design mode has a physical optics propagator (POP) tool that allows one to work with the properties of laser beams. The geometric optics raytrace does not incorporate diffraction effects in image formation. The geometric images of the rays in the 1250mm lens system are spots with dimensions on the order of a few nm while the actual diffraction image on the CCD detector is on the order of 200 microns full-width-half-maximum (FWHM). We can use the POP tool to simulate the actual image produced by the laser beam imaged through the lens in the LTP-II system. To do this properly, we need to account for the full optical path from laser source to the detector plane. The reflection of the beam from the SUT requires that we unfold the system to produce a sequential component model. The POP model for the LTP-II is shown to scale in Fig. 6. The PBS is shown twice on either side of the SUT, since the beam is incident on the SUT after the first pass through the PBS and then passes through the PBS again after reflection from the SUT. Only after this encounter does it pass through the lens. No splitting of the rays occurs in this SC model.

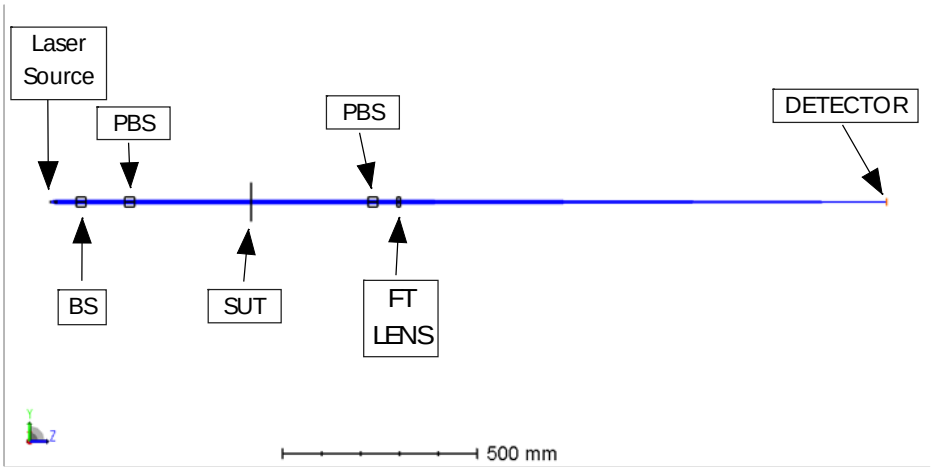

Figure 6. Simplified model of LTP-II for Sequential Component (SC) mode POP analysis. Rays traverse each element only once with no splitting. The PBS is shown twice because it is traversed again by inbound rays after reflection from the SUT.

Gaussian beams are defined by a beam waist parameter, w_0, a divergence angle, θ_0, and a wavelength, λ. The relationship is

$$\theta_0 = \frac{\lambda}{\pi w_0} \tag{2}$$

In our case, the laser beam source is the end of the single-mode fiber core. The beam waist parameter is approximately equal to the fiber core diameter. The fiber manufacturer provides nominal values for these parameters. For the single-mode fiber used in the ALS LTP-II, the nominal mode field diameter ($1/e^2$ in near field) is 4.5 ±0.5μm @ 630nm with a divergence given by the numerical aperture, NA = 0.120. ZOS uses the radius of the $1/e^2$ point as the beam waist, so for ZOS purposes, we use as the initial beam width w_0 = 2.25 μm. This is a nominal number and will be adjusted to give results closer to what are actually observed. The output of the fiber is collimated by a Thorlabs collimating lens with an 11 mm focal length and aperture diameter of 7.2 mm. With these parameters, we can use the Paraxial Gaussian Beam Calculator (PGBC) tool to calculate the properties of the laser beam as it propagates through each surface. We get the beam sizes shown in Table 1.

Table 1. Laser beam parameters computed with the Paraxial Gaussian Beam Calculator tool.

Component	**Beam Radius [μm]**
Fiber core	2.25
Collimator lens	985.
FT Lens	991.
Detector	255.

Now we can use the Physical Optics Propagator (POP) tool to see what the image looks like on the detector with the PGBC parameters. The image on the detector is shown in Fig. 4. The beam radius is the same as calculated by the PGBC – 255 μm – as it should be. Note that ZOS uses an unconventional definition for Gaussian beam radius. See the Appendix for the explanation.

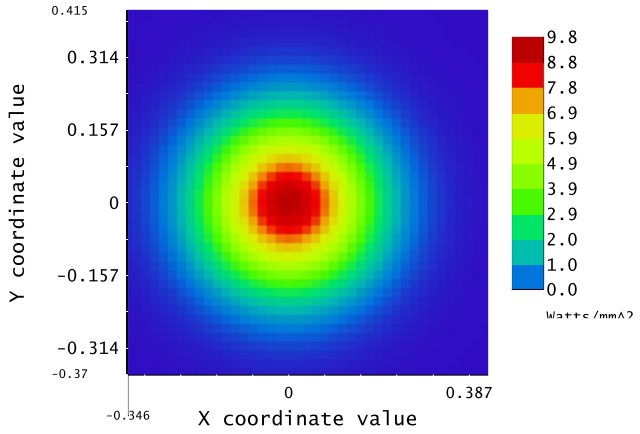

Total Irradiance surface 10

LTPII lens Gaussian laser, 3/3/2019
Beam wavelength is 0.63300 µm in the media with index 1.00000 at 0.0000 (deg)
Display X Width = 9.8453E+00, Y Height = 9.8453E+00 Millimeters
Peak Irradiance = 9.7939E+00 Watts/Millimeters^2, Total Power = 1.0000E+00 Watts
Pilot: Size= 2.5495E-01, Waist= 2.5226E-01, Pos= 4.6301E+01, Rayleigh= 3.1582E+02
Beam Width X = 2.54954E-01, Y = 2.54954E-01 Millimeters

Figure 7. Physical Optics Propagator result for image irradiance in the FT Lens focal plane.

Now look at the actual measured LTP-II beam widths to fine-tune the model parameters. A typical single-beam image on the detector is shown in Fig. 8. The detector in this case is a CCD camera with 7.4 µm pixels.

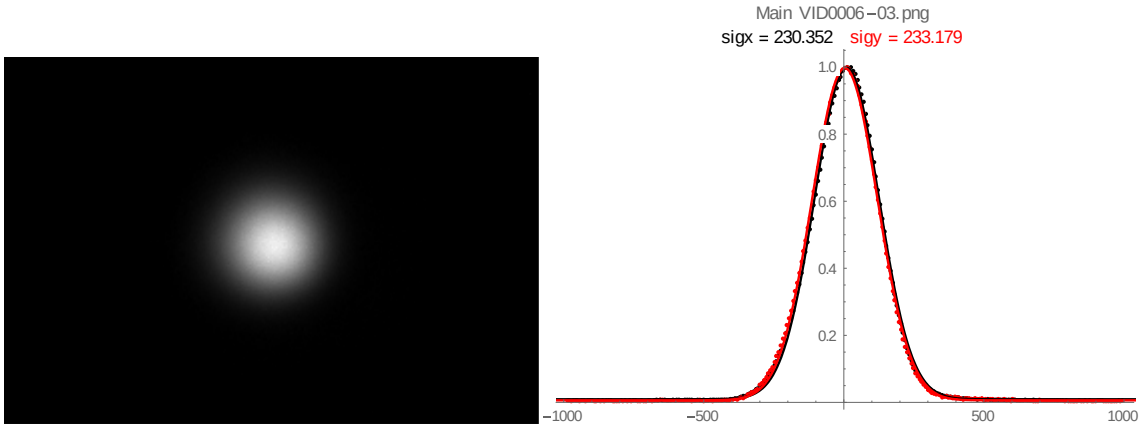

Figure 8. Actual LTP-II beam spot image recorded on CCD camera. Beam radius in y-direction is 233 µm. The sigma values in the plot title are in terms of the ZOS beam radius definition, which is the radius of the $1/e^2$ point on the curve.

Using the ZOS convention, the beam radius of the measured single-beam image at the focal plane of the FTL is 233µm. This is the profile in the tangential plane of incidence of the SUT, which measures the slope of the surface. The sagittal direction profile is not relevant to the measurement simulation.

Now look at the beam incident on the FTL. The size of the beam at this point determines the size of the spot at the focus of the lens. Since it is difficult to record the image at the FT lens inside the optical head, we look at the beam in the REF arm as it exits the optical head. The precise location is not important because the laser beam is diverging very slowly at this point. An average of several beam width measurements over a range of distances in the REF arm results in an average measured beam radius of 863µm.

Now, the actual image spot radius is 233µm but the initial simulation with a source radius of 2.25µm gives an image spot of 255µm. Since 2.25µm is only a nominal value, we are free to adjust the source radius so that the PGBC gives the observed spot size. We need to adjust the source size from 2.25µm to 2.10µm. This gives an image size of 238µm, which

is close enough to the observed value of 233μm. The propagating beam radius at the FT lens, however, goes up to 1.05mm from 0.863mm. This is not a significant issue, as what really matters is the size of the image on the camera, and the SC model agrees with the observed image size with the current set of parameters.

3.5. Single Beam vs. Double Beam Mode

The original PBI and LTP-II utilized the laser beam split into two collinear beams, adjusted to produce a single fringe minimum in the interference image on the detector. The two right angle prisms are set up to produce zero optical path difference between the two beam components when they are fully overlapped. When they are separated by translating one of the prisms, an interference pattern is generated similar to the classical double-slit pattern. If the translation of the upper prism were exactly parallel to z-axis, the optical path difference would remain at zero and the interference fringe would have a central maximum. In order to produce a central minimum, one of the beams needs to acquire a phase shift of one-half wave, λ/2. Fortunately, the translation stage is never aligned perfectly with the z-axis, so when it is translated by a millimeter in z, it acquires a small distance in y, on the order of microns, which is enough to produce the central minimum phase shift. Unfortunately, stability of the prism translation stage is also not very good, resulting in slow drifting of the position of the minimum. This contributes to the overall systematic error in the system and is very difficult to correct [ref]. It is possible to use a phase plate inserted into the laser beam to produce a fringe minimum [ref], but we have determined that single beam mode, with no interference pattern, produces the same slope angle measurements as the double beam mode. Hence, all modeling can be done in single beam mode. This actually simplifies the raytracing process, requiring fewer rays to be traced, speeding up the process. The recent LTP500 optical designs, similar to Fig. 2, no longer incorporate the RAP-BS component group for generating dual beams.

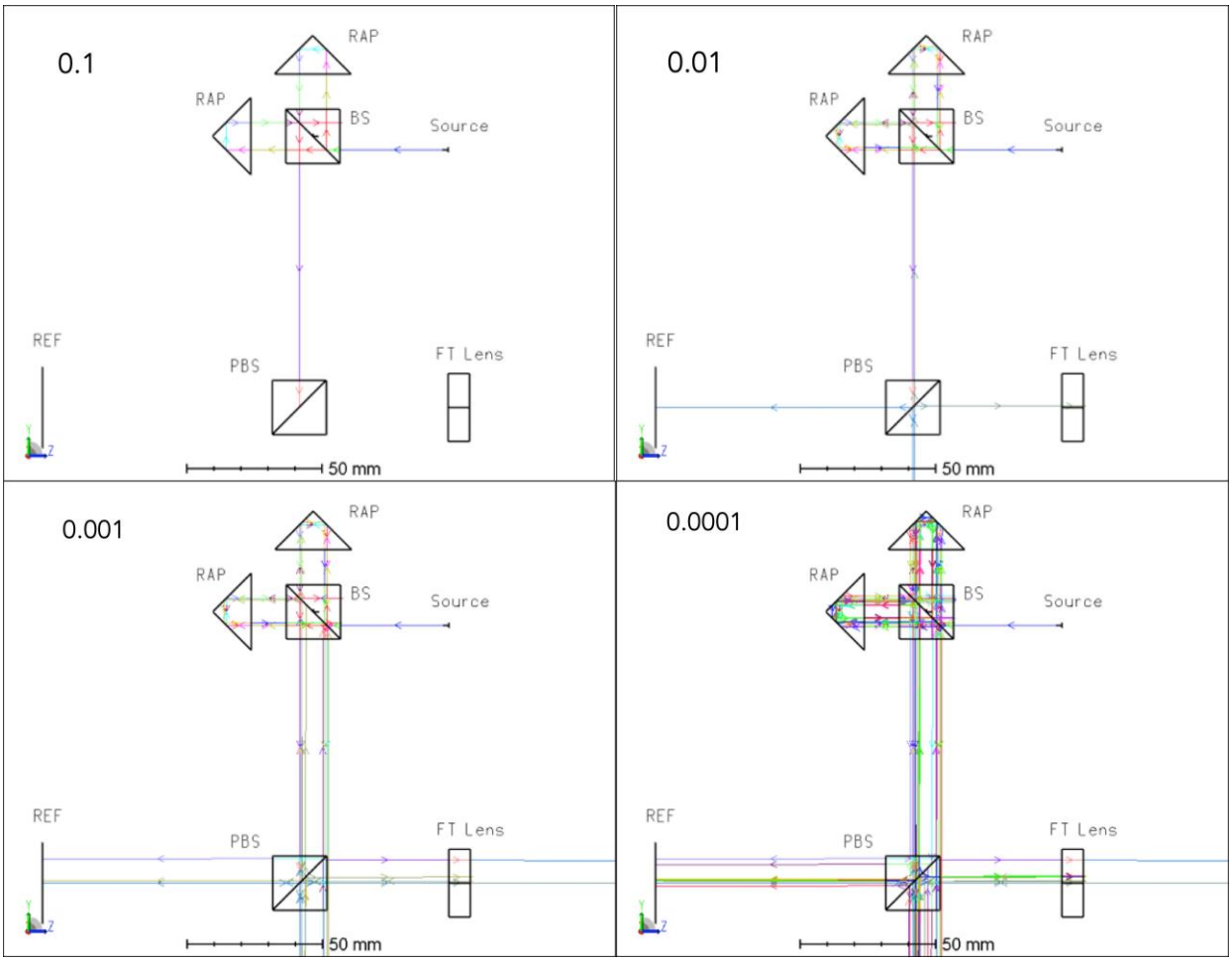

Figure 9. Ghost ray production in NSC mode as a function of Minimum Relative Ray Intensity. The is a single ray. As the MRRI threshold decreases, more ray segments and branches are produced.

NSC mode also produces diffraction images by Fourier transform propagation of wavefronts between surfaces and also by Huygens summations of optical path lengths. We use these tools to view the spot intensity on the detector plane. We analyze the spot shapes to look for distortion produced by the ghost rays with a *Mathematica*™ code that fits a Gaussian function to the image and extracts the center coordinate. ZOS has an internal programming language, ZPL, similar to BASIC, that allows one to build macros that execute multi-step raytracing and analysis functions. We use these macros to perform scan simulations by tilting or translating the SUT and recording the image intensities in detector viewer files. An example of two scan sequences is shown in Fig. 10. The upper panel has the MRRI threshold set at a high value (1E−2) to eliminate ghost rays. The upper panel has the threshold set to a low value (1E-5) to include ghost rays. The goal of this simulation effort is to identify the sources of ghost rays and develop way to mitigate the harmful effects.

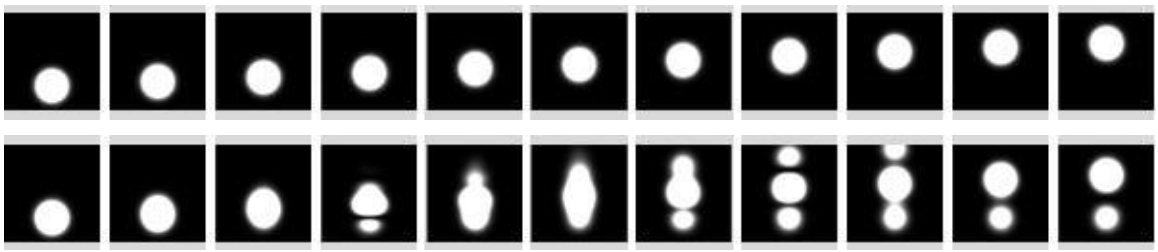

Figure 10. A scan sequence simulation by tilting the SUT over a small angular range. Images with no ghost rays (upper) and with ghost rays (lower) showing distortion effects.

The image sequences shown in Fig. 10 are the result of a macro that tilts the SUT in uniform angular increments. We call this a "calibration" scan, as the resulting images should lie along a straight line, and any deviation determines the calibration correction at that angle. Fitting the two calibration scans in Fig. 10 to straight line functions and subtracting the fits, we plot the residuals in Fig. 11. One can see that the ghost ray distortion produces microradian-level calibration errors. The undistorted residuals are in the nanoradian range – too small to be seen on this scale.

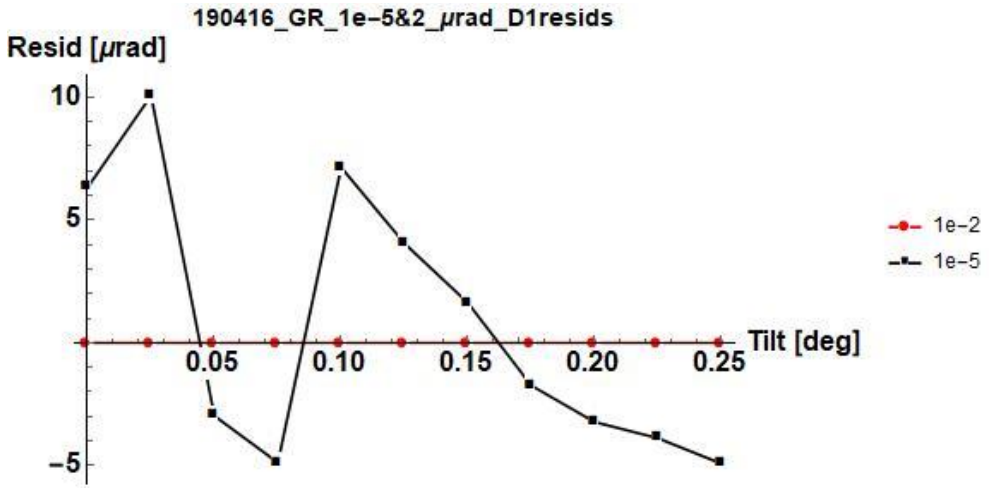

Figure 11. Residuals from linear fit to the calibration scans in Fig. 10. The undistorted 1E-2 image residuals on the order of nanoradians are too small to see at this scale. The ghost rays produce microradian level distortions in the calibration.

3.6. Ghost ray mitigation

The most obvious source of ghost ray images is back reflection from the glass surfaces. Typical glass has a reflectivity of about 4% at normal incidence at visible wavelengths. A simple MgF_2 antireflection (AR) coating cuts this down to about 1%. ZOS has a large number of coatings available that can be applied to different glass surfaces to reduce back reflections. If we apply the MgF_2 coating to all of the glass surfaces and trace a single ray with MRRI set to 1E-5, we get the result shown in Fig. 12 on the left.. The SUT is tilted slightly here to separate the ghost rays. This does not even include the rays from the REF arm. No ray filter is applied so this plot shows all of the ray segments and branches produces by back reflections. An absorbing mask is inserted below the BS cube to intercept rays passing up through and by the PBS. One

can see the tremendous number of ray segments generated by all of the glass surfaces. Two ghost rays make it past the lens. Other multilayer coatings can be applied to reduce the back reflections by factors of ten or more, depending upon the complexity of the coating prescription.

Another ghost ray mitigation strategy is to purposely misalign the optical components by rotating them to cause the ghost rays to walk off the detector. If we rotate the RAP-BS group by 0.3º about the X-axis and counter rotate the PBS, the ghost rays miss the ends of the detector, but the chief ray returned from the SUT exits the PBS parallel to the original optical axis but displaced a small amount in Y. To recenter the chief ray in the PBS and in the FT lens, we need to shift the PBS in Z by a few mm and shift the FT lens down by a small amount. The optimized layout is shown on the right in Fig. 12. Note that the SUT is oriented normal to the global Y-axis, which is the 0mrad tilt condition. The chief ray beam from the PBS is now incident on the SUT at a slight angle, so the PBS is shifted to put the return beam in its center. If we do another calibration run over the full angular tilt range, we can see from the detector images that the ghost image separates nicely from the main image in Fig.13. But when we fit the image spot to the Gaussian function and look at the calibration curve residuals, we see that there is still some low-level distortion in the positive angles in Fig. 14. Increasing the rotation angle of the BS cubes from 0.3º to 0.4º eliminates this ghost ray contamination.

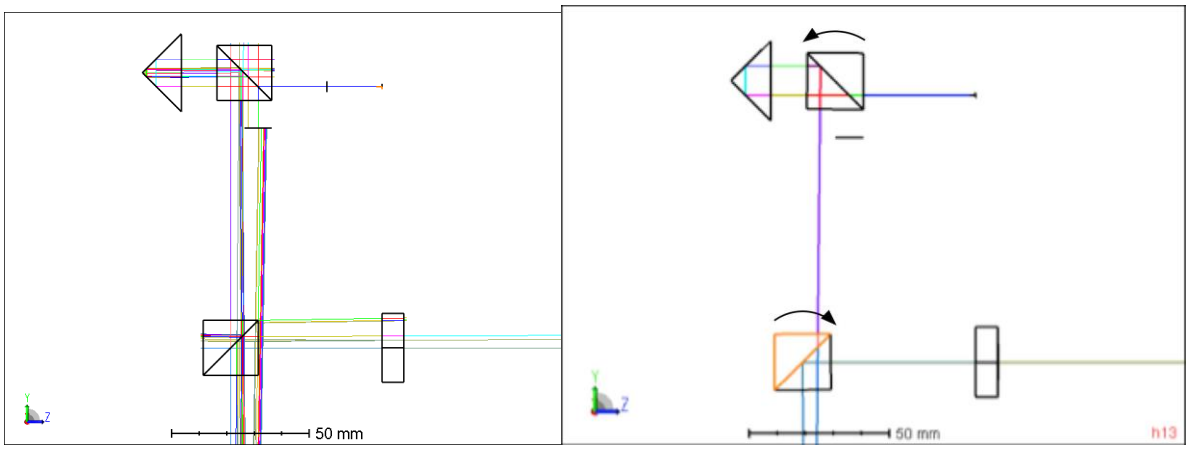

Figure 12. (Left) Ghost rays from a single source ray with simple AR coatings applied to all glass surfaces. The SUT is tilted slightly to separate ghost rays from the central ray. MRRI = 1E-5. (Right) Counter-rotating the BSgroup and the PBS by 0.3º eliminates ghost rays with the SUT at 0mrad tilt.

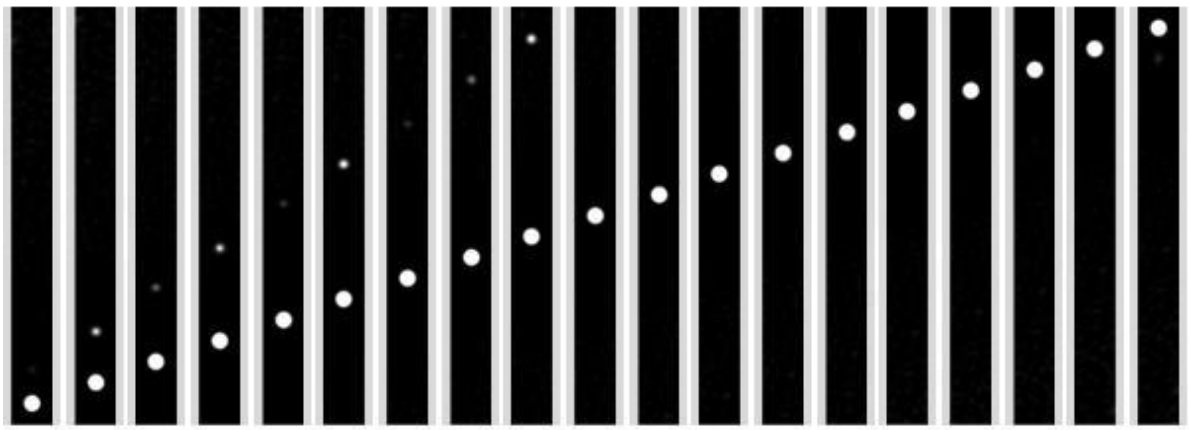

Figure 13. Full tilt angle calibration run from -4.5 to +4.5mrad showing the ghost ray image separating from the main image as the SUT tilt angle increases from left to right.

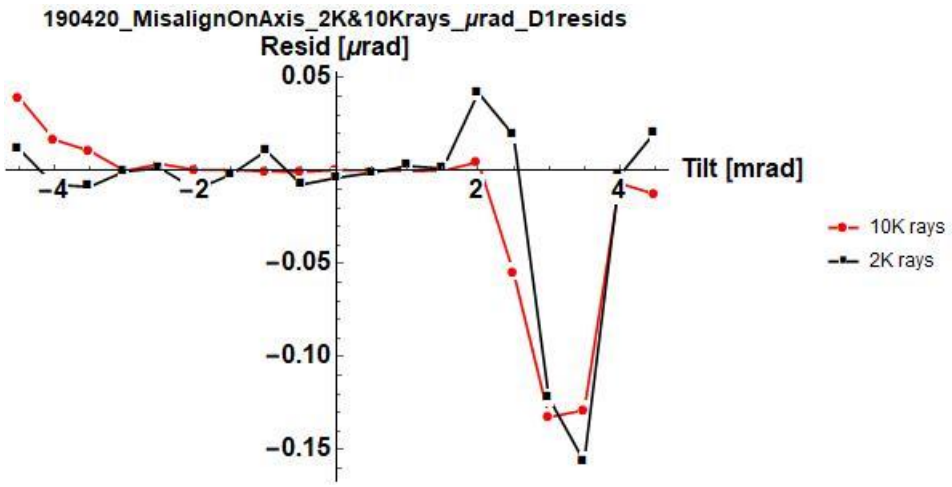

Figure 14. Residual distortion error in the 0.3º misaligned system caused by low-level ghost rays in the positive angle region. The distortion is not visible to the eye in the Fig. 13 images. Two runs were done, one with 2K rays and one with 10K rays to assess the effect of number of rays traced on the image position.

Back reflection from the CCD detector surface is another ghost ray source. The detector is usually modeled as an absorber surface – no rays exit from the surface by transmission or reflection. In actuality, the detector is not a perfect absorber. It will produce some back reflected rays that reach the FT lens and can be a source of ghost rays back to the detector, especially for rays close to the optical axis. We can see this happen by doing a small angle calibration run over an angular range of ±0.5mrad. Fig. 15 shows the results of 3 runs with different detector-lens reflectivity conditions. The largest error occurs when the detector is made to be a MIRROR surface so it reflects everything incident on it. Only the rays near the normal incidence condition back reflect from the FTL which has a simple AR coating on it. Smaller error occurs when the detector surface is made into a 5% reflector. The minimum error occurs when a WAR "W" coat (half wave of La_2O_3 and a quarter-wave of $MgF_{2)}$ AR coating is added to the FT lens. Although the residual error is small with the better FT lens coating, there is still some distortion in the image due to back reflection from the detector. Taking a cue from the earlier solution for mitigating ghost rays originating in the BS and PBS cubes, we can rotate the detector about its vertical axis by 0.6º (the Y-axis in the layout) to make the back-reflected rays miss the FT lens. So rotate the detector by 0.6º and make another small angle calibration run. Also change the coatings on the glass surface to a better HEAR1 (high efficiency AR) which is a 3-layer coating with less than 0.25% reflectance from each surface. The result in Fig. 16 shows no distortion effects down to the nanoradian level in the small angle range. The final LTP-II optimized model incorporates counter rotation of the BS group and the PBS by 0.4º about the X-axis and rotation of the CCD detector by 0.6º about the Y-axis.

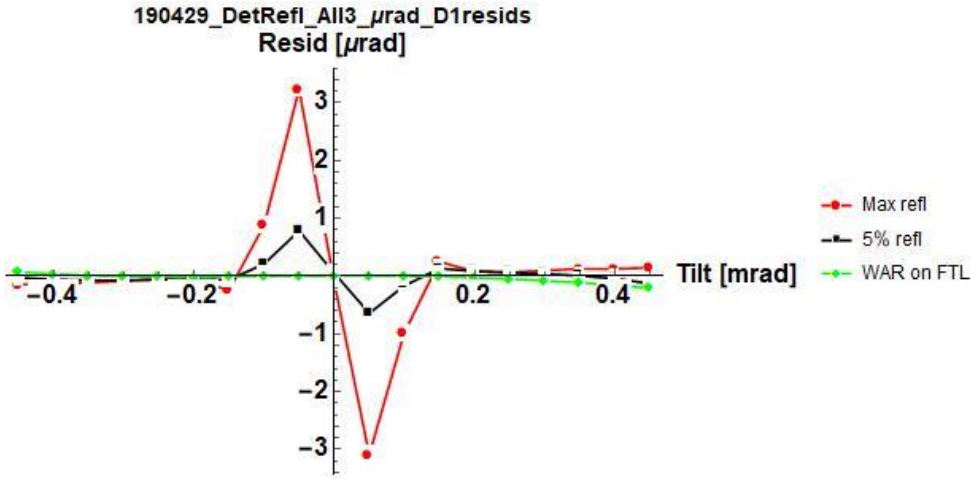

Figure 15. Residual spot center error near 0 mrad tilt angle for different FT lens – detector reflectivity conditions.

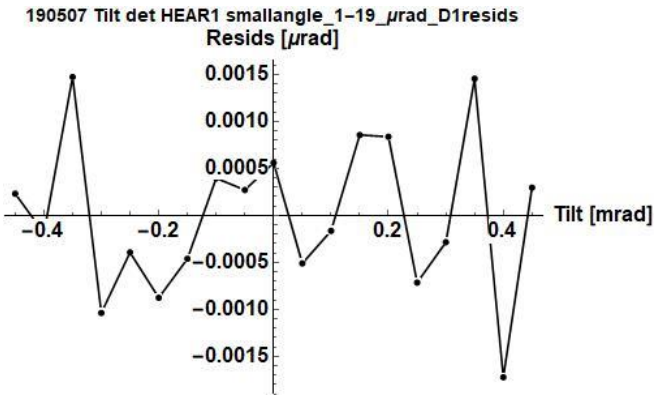

Figure 16. Residuals with the HEAR1 coating on all glass sirfaces in the small tilt angle region shows no significant distortion at the nanoradian level.

3.7. LTP-II REF Beam Considerations

Up to this point in the LTP-II modeling the REF beam has been turned off. The counter rotation of the BS and PBS returns the SUT beam to the horizontal optical axis centered on the FT lens. The REF arm beam, however, does not get counter rotated and maintains the tilt angle imposed by the PBS. This causes the REF beam to walk across both the reference mirror surface and the FT lens aperture. To see what problems may arise from this configuration, we run a simulated scan where the REF arm moves from 100mm to 500mm away from the PBS. The following 3 frames in Fig. 17 show the REF arm rays for distances of 100, 300, and 500 mm distances. One can see that the return beam walks across most of the aperture of the PBS and lens as the distance increases to 500mm. Although the return beam angle is constant, the image moves on the detector because the lens is not designed to image a constant-angle beam translated across the lens aperture with low distortion. The total scan range is also limited to 400mm because the return beam vignettes beyond the 500mm distance. Because the outgoing REF beam is tilted by 0.4º, it also walks across the face of the reference mirror. Proper system design would keep the REF beam fixed at the same spot on the reference mirror so as not to introduce distortion into the REF image due to surface irregularities. It is possible to keep the REF beam position constant on the reference mirror with the addition of two fold mirrors, as shown in Fig. 18. The two mirrors counteract the tilt imparted to the REF beam by the rotated BS cube, making the beam exiting the optical head again parallel to the translation axis. But the return REF beam is given the initial rotation angle as it retraces its path through the fold mirrors. Exiting the PBS, the REF beam is at a 1.558º (0.0272rad) angle relative to the optical axis of the lens. It come to a focus 34mm away from the center of the detector field of view, which puts it off the edge of the detector by 11.5mm. A separate detector would be needed to record the REF beam. The difficulty in utilizing the REF beam for correcting the errors in the carriage motion is a good argument for utilizing an external autocollimator for this purpose.

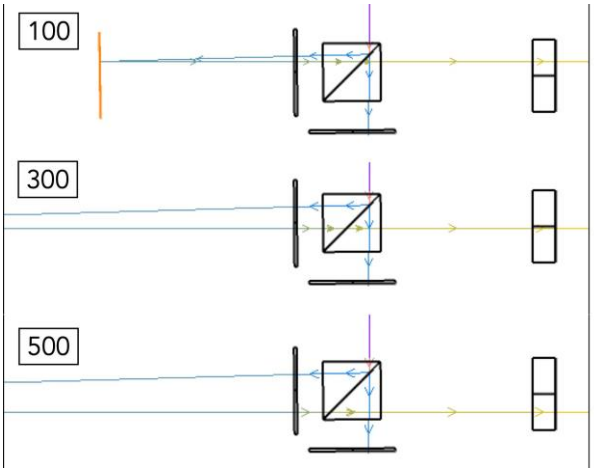

Figure 17. REF beam walks across the PBS and FT lens as the optical head is translated with the rotated BS components in LTP-II model. Distance of reference mirror away from PBS is indicated.

Other solutions to the tilted REF beam are possible. Tilting the entire optical head to make the REF beam collinear to the x-axis translation direction will center the REF beam on the detector, but it introduces a small off-normal incidence angle into the SUT beam. This has a negligible effect on measurement accuracy. A tilt angle of 0.4° is the current solution employed by the ALS LTP-II. Other solutions employ the use of thin plate beamsplitters, but space does not allow us to pursue these solutions in this paper.

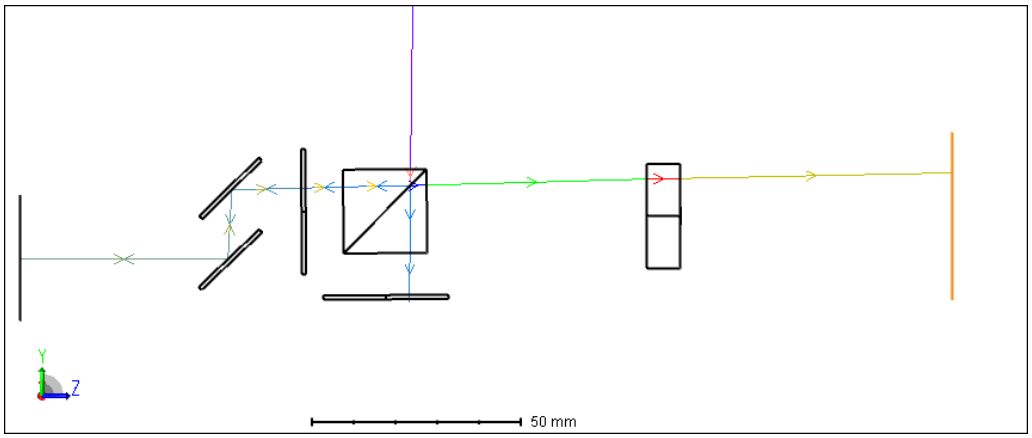

Figure 18. Optimize REF arm with two fold mirrors to produce horizontal beam. The return beam exiting the PBS is at an angle that is focused 34 mm from the center of the detector (not to scale).

4. LTP500 DESIGN

The most recent design for the LTP optical head is shown in Fig. 2. It is a simplification of the original LTP-II design. Operating in single beam mode, it no longer incorporates the RAP-BS group. Rather, the laser beam is directly incident on the PBS from the left. The reference mirror is off to the right so there is no deviation between the incident beam and the REF beam direction, even if the PBS is rotated. The SUT is below the PBS and the FT lens is above the PBS. Not shown are two folding mirrors after the lens that route the beam to the detector (also not shown). Also not shown are the polarizers between the laser source and the HWP that act as an intensity control and produce a linear polarized beam. The HWP rotates the linear polarization so that the relative intensities of the SUT and REF beams exiting the PBS can be adjusted. This is the BALANCE control between SUT and REF arm intensities.

The newer systems utilize CCD and CMOS cameras with smaller pixels than those in the original LTP-II. This enables the use of lenses with shorter focal lengths without sacrificing resolution. Also, the angular acceptance range can be increased to accommodate mirrors with shorter radii, since the detector dimensions remain the same. The most recent lens design was done in 2014 as part of an international LTP upgrade project. This lens has a 500mm effective focal length with a SUT slope angle measurement range of ±10 mrad. This results in a ±20 mrad field angle acceptance range at the lens. The lens was optimized to produce minimum distortion over the indicated field angles for SUT distances between 300 and 400 mm. The parameters for this lens design are shown in Table 2. Note that surface radius is positive if the center of curvature (CoC) is to the right of the vertex, negative if the CoC is to the left of the vertex.

Table 2. LTP500 2014 cemented doublet design.

Surface	Comment	Radius	Thickness	Glass	Semi-Diameter
0	Object		Infinity		0
1	Aperture stop		300.000		1
2	PBS CUBE	Plano	40.000	S-BSL7	20
3	SPACE TO LENS	Plano	30.000		20
4	Lens 1 front	1578.28	4.000	S-BSL7	15
5	Lens interface	-138.90	10.000	S-LAH53	15
6	Lens 2 back	-215.13	499.476		15
7	Image plane				10

The original 2014 cemented doublet design incorporates a PBS cube that is 40mm thick. However, the model used in this paper uses a 30 mm thick cube. The advantage of a smaller PBS cube is less glass thickness, which is one of our basic design principles. The primary effect of this difference is to shift the optimum SUT distance for minimum distortion. Taking a lesson from the LTP-II optimization process, the first order of business is to locate the SUT at the optimum distance so as to minimize large-angle calibration error. The Minimum Relative Ray Intensity (MRRI) parameter is set to 1E-02, which is a high threshold, to eliminate interference from ghost rays at this point in the analysis. With a flat SUT, several calibration tilt angle runs were made over a SUT distance range from 260 to 500 mm. Note that this distance to the SUT is measured from the origin of the global coordinate system which is located at the center of the PBS. The resultant calibration residuals are shown in Fig. 19. One can see that a 3rd-order polynomial term dominates the residual error curves, and it changes sign somewhere around the 420mm distance. Additional calibration runs show that the optimum SUT distance is 424mm with a maximum distortion less than 5 nrad. The scale factor for the LTP500 system is 5.4 μm per pixel, which is 5.4 μrad of surface slope per pixel.

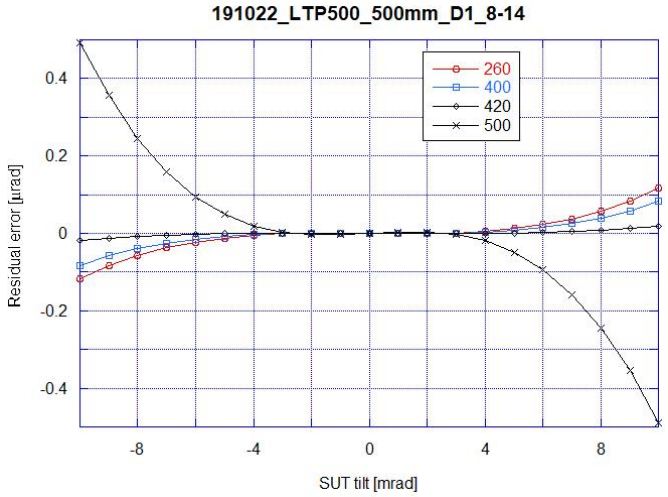

Figure 19. Calibration run residuals as a function of SUT distance.

The residuals for the 424mm SUT calibration run with the threshold MRRI set to 1E-02 to eliminate ghost rays are shown in Fig. 20 on the left. If we lower the threshold to 1E-06, we see that the distortion increases drastically by a factor of 100. So there is significant distortion of the image spot by ghost rays that needs to be corrected.

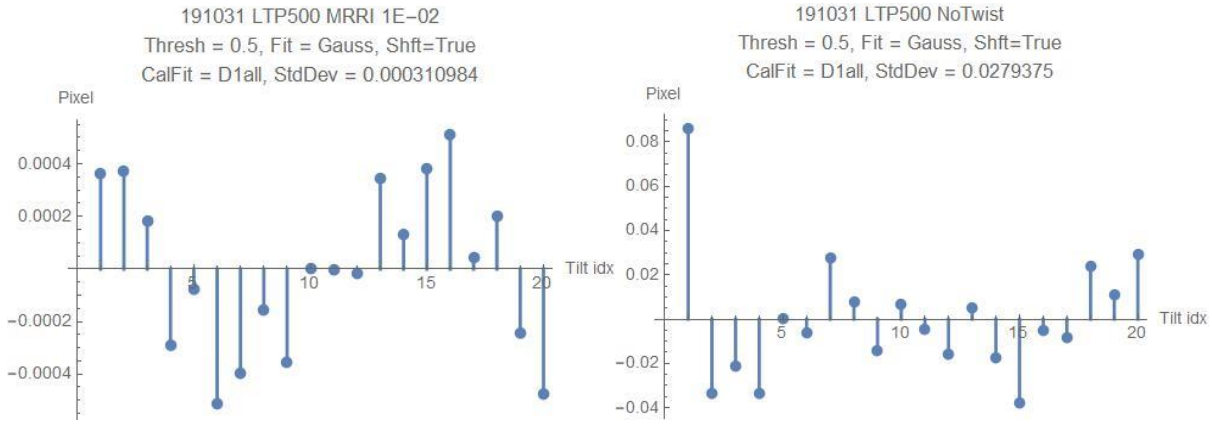

Figure 20. Tilt calibration runs for the 2014 cemented doublet system with no ghost rays (left) and with ghost rays (right). Note ordinate scale is a factor of 100 greater on plot on right.

Taking a cue from the LTP-II 1250-mm-FTL system optimization, we suspect that rotating the PBS will reduce ghost ray interference. However, the symmetry of the system suggests that, rather than tilting about the global X-axis, we should look at the effects of twisting the PBS about the Y- and/or Z-axes. If we twist the PBS by 0.1° about the Z-axis, the outbound REF beam is not deviated and stays centered on the REF mirror as the optical head is scanned. When both the

SUT and REF beams come back through the PBS, they are deviated in opposite directions in X and form image spots that are well separated by about 2 mm. The beam incident on the SUT is at a small fraction of a degree angle off normal, which can be easily compensated for by slightly tilting the SUT mirror. If we run the tilt calibration over the ±10 mrad surface tilt range with MRRI set to 1E-02 (no ghost rays), we get the ideal low distortion residuals in Fig. 21 on the left. However, if we lower the MRRI threshold to 1E-06, we see the distorted residuals on the right. We need to track down the sources of this ghost ray interference and minimize them.

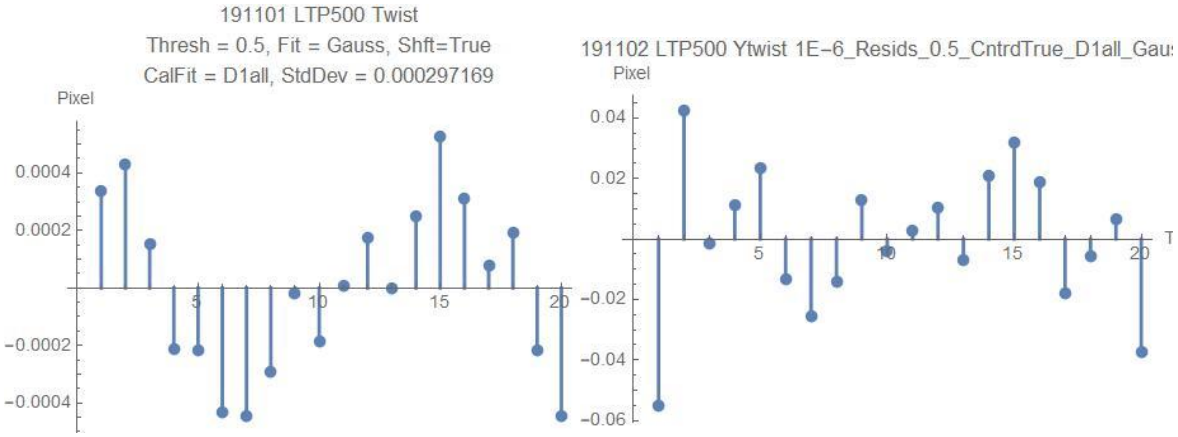

Figure 21. Calibration run residuals for the LTP500 cemented doublet with the PBS twisted by 0.1° about the global Z-axis. Left panel is with MRRI = 1E-02 to suppress ghost rays. Right panel has MRRI = 1E-06 to include ghost rays distortion. Vertical scale on right is 100 times that on the left.

Using the Ray Database Viewer, we can see what elements are producing multiple ray branches and then adjust the anti-reflection coatings to reduce the intensity of the back-reflected rays. We need to use the Reflection vs. Angle plot to see what the reflectivity is for a given coating on a particular substrate. Incidence angles are always less than 3° so the reflectivity of the coating depends only on the index of refraction of the substrate. Some coatings are optimized for high index materials, like the back element of the FT lens; others are best for low index materials. By trial and error, we can find the best AR coatings for each element.

- For the RAP Homosil™ material, the best coating is THOR633, which gives a reflectivity of 0.05%.
- The FT lens front element is S-BSL7 with a low index and has a THOR633 coating applied, which gives a reflectivity of 0.0008%.
- The back element is S-LAH53 (high index) and has lowest reflectivity with a ZEC_V633_SF11 coating, with a reflectivity of 0.075%.
- Put the THOR633 coating on the surfaces of the quartz waveplates. The reflectivity of these surfaces becomes 0.004%.

With the above coatings, the ghost ray intensities fall below the 1E-06 MRRI threshold level, so there are essentially no ghost rays that reach the detector.

For completeness, look at the REF spot position as the reference mirror distance is increased from 100 to 1000mm. The simulated scan residuals are shown in Fig. 22. The result is essentially zero error. This confirms our twist angle solution. The standard deviation in pixels corresponds to 0.1 nrad error. This LTP500 optical system provides a solid, stable reference beam.

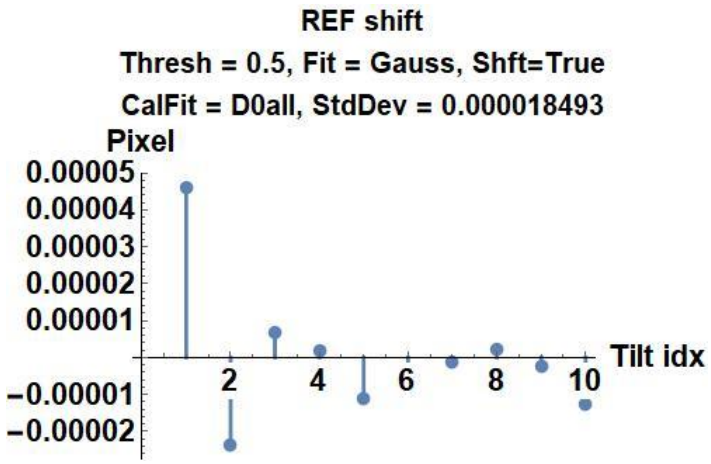

Figure 22. REF beam image for LTP500 system with 0.1° twist about Z-axis and with optimized coatings. The standard deviation corresponds to 0.1nrad error.

4.1. GridPhase Surface - Tolerancing

All the model results to this point are for an ideal system: all components are perfect. ZOS has the capability of importing actual wavefront data produced by commercial interferometer software. We have transmitted wavefront data for the cemented doublets that were measured by a Zygo Fizeau interferometer. We can convert the Zygo .DAT or .XYZ file data into a ZOS GridPhase surface and add it to the SC lens model to calculate the effect of the wavefront errors on the physical optics beam spot image. An example of a gridphase surface generated by the transmitted wavefront data for one of the cemented doublets, sn14, is shown in Fig. 23. The pupil diameter for this surface is 20mm with grid pixels of 0.110mm. The clear aperture (CA) is a 5mm wide strip down the center. The wavefront error in the CA is on the order of 0.1 wave peak-to-valley (PV). Converted to phase error in height units, it has an RMS value of about 19nm.

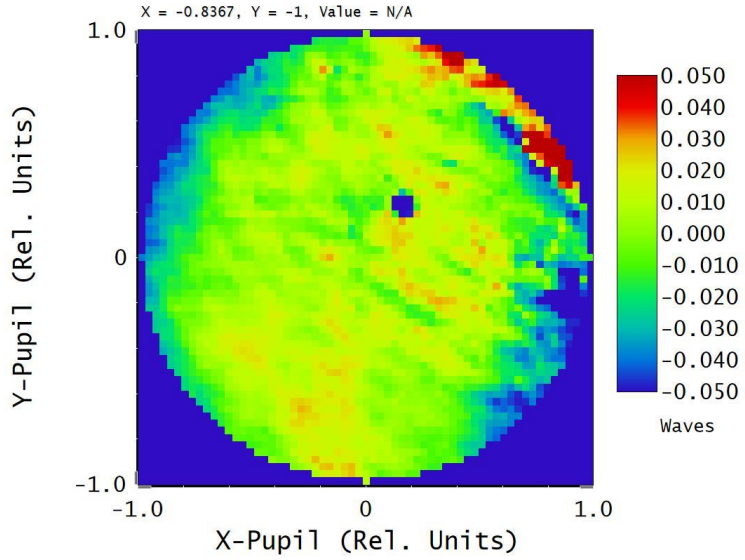

Wavefront Function Sx: 0.0000, Sy: 0.0000, Sr: 0.9000	
LTP500 single element aspheric, 7/25/2020 0.6330 µm at 0.0000 (deg) Peak to valley = 0.2339 waves, RMS = 0.0196 waves. Surface: 1 (sn14central20mmMask_XYZ_GridPhas) Exit Pupil Diameter: 2.0000E+01 Millimeters Tilt Removed: X = 0.0801, Y = 0.1978 waves	Zemax Zemax OpticStudio 18.9 Doublet_FizeauTest.ZMX Configuration 3 of 3

Figure 23. Wavefront map of the sn14 lens gridphase surface. PV error in the CA is about 0.1 wave or 19nm.

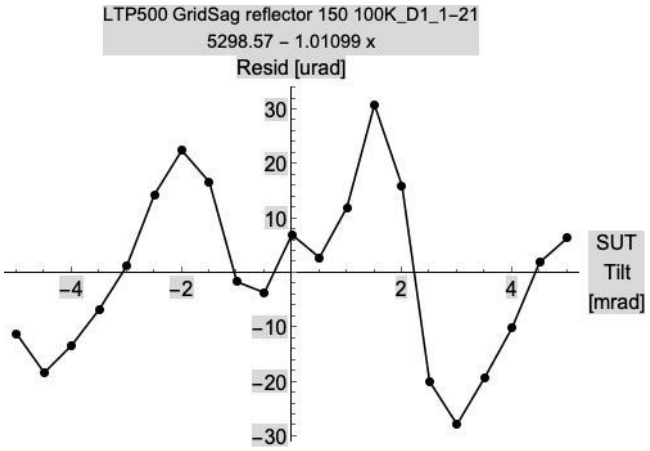

Figure 24. Residuals for tilt calibration run with lens sn14 gridphase wavefront surface added to the model. PV error is 60μrad.

The residual errors for a tilt angle calibration run with the gridphase surface in Fig. 23 are shown in Fig. 24. The PV error is 60μrad. This error is orders of magnitude greater than the ideal distortion level, which is in the nanoradian range. We can measure the actual distortion produced by the real lens by setting up a laser beam scan across the lens aperture while recording the spot image on a CCD camera. With the camera at the lens focal plane mounted with the lens on the granite slab Y-stage of the XROL OSMS[22], the image should remain stationary as the lens is translated across the laser beam with no tilting. The results of several Y-slab scans, shifting the lens by 1 mm in X between each about the centerline, are shown in Fig. 25. The scale factor for converting microns to microradians is 1.0, so numerically the vertical scales for Figs. 24 and 25 are the same. One can see that the PV variations of the laser spot are around 3 μm, while the grid phase model shows the variations to be an order of magnitude greater. More work is needed to understand the source of this discrepancy.

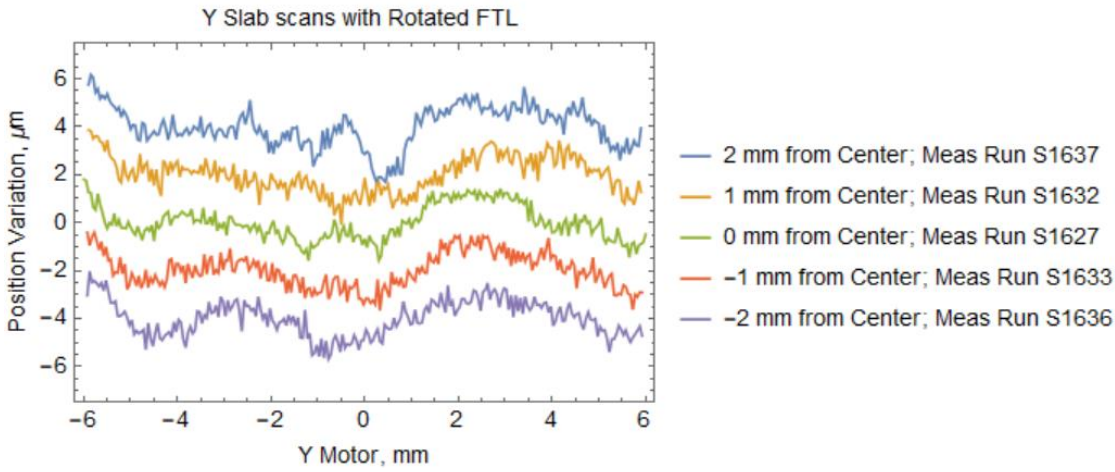

Figure 25. Scan laser beam across the lens aperture at constant incidence angle. Ideal image should be straight line. The measured variation is an order of magnitude less than the gridphase model predicts.

5. ASPHERIC SINGLET LENS

The measured transmitted wavefront error in the cemented doublet lenses leads us to reconsider the design of this lens. It is comprised of two separate elements of different materials with different thicknesses, with 4 spherical surfaces, with the two mating surfaces needing to have precise complementary curvatures. These elements require a significant effort to select the best quality blanks and grind, polish, coat and cement together the 2 elements. All of these interfaces are

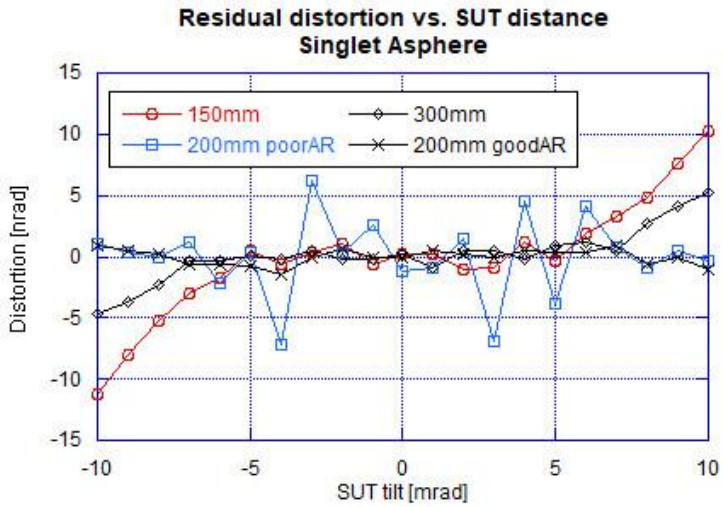

Figure 26. Distortion results for singlet asphere for various SUT distances. Optimized for 200mm. Two runs for 200mm: one with poor AR coating (WAR), one with the good AR coating (OPTIMAX-V633-1_46).

potential sources of wavefront error. As a way to reduce the number of error sources and to take advantage of recent developments in optical fabrication technology, we investigated the use of adding an aspheric surface to the lens. The 7 degrees of freedom needed to control distortion in the doublet are reduced to 4 for the aspheric singlet. Replacing the doublet in the LTP500 SC model, we can quickly optimize the system for a nominal SUT distance range of 150 to 300 mm for the ±20 mrad field angle range. Inserting this lens into the LTP500 NSC model, tilt angle calibration runs for three SUT distances give the residual error in Fig. 26. An OPTIMAX-V633-1_46 coating with R = 3.0E-05 is applied to each surface. The results for the 200mm run with a poor WAR coating with R = 0.02 on the lens shows the effect of ghost rays on the residuals. For the most part, the distortion is below 10 nrad over the entire measurement angle range over the full SUT distance range. This is much better performance than the distortion shown for the cemented doublet in Fig. 19.

Table 3. Tolerance list for aspheric singlet lens.

Num	Type	Int1	Int2	Nominal	Min	Max	Units	Comments
1	TWAV	0.00	0.6328				µm	Default test wavelength.
3	COMP	8	0	0.00	-10.	10.	mm	Comp adjusts image plane position
4	CPAR	8	3	0.00	-8	8	mm	Comp on image x-tilt
6	TTHI	5	6	9.80000	-0.15	0.15	mm	Default thickness tolerances.
7	TCON	5	-25.70	-1.0	1.0			Conic on front surf
10	TRAD	5	1	876.08299	-0.10	0.10	%	Default radius tolerances.
11	TRAD	6	1	-308.3097	-0.10	0.10	%	
13	TEDX	5	5	0.00	-0.20	0.20	mm	Default surface dec/tilt tolerances 5.
14	TEDY	5	5	0.00	-0.20	0.20	mm	
15	TETX	5	5	0.00	-0.020	0.020	Deg	Wedge TIR deg
16	TETY	5	5	0.00	-0.050	0.050	Deg	"
17	TEDX	6	6	0.00	-0.20	0.20	mm	Default surface dec/tilt tolerances 6.
18	TEDY	6	6	0.00	-0.20	0.20	mm	
19	TETX	6	6	0.00	-0.050	0.050	Deg	Wedge TIR deg
20	TETY	6	6	0.00	-0.050	0.050	Deg	"

To finalize the lens specification parameters, we use the Tolerance tool in the SC model. The list of relevant tolerance operands is shown in Table 3. Compensators are placed on the focal plane distance and image plane tilt so that these parameters are adjusted to minimize the distortion merit function during each Monte Carlo run. The distortion vs. field angle results of 100 Monte Carlo runs with random combinations of these parameters is shown in Fig. 27. One can see that with the compensators, the maximum distortion is ±30 nm at the extremes of the angle measurement range. This distortion can be easily corrected by calibration measurements.

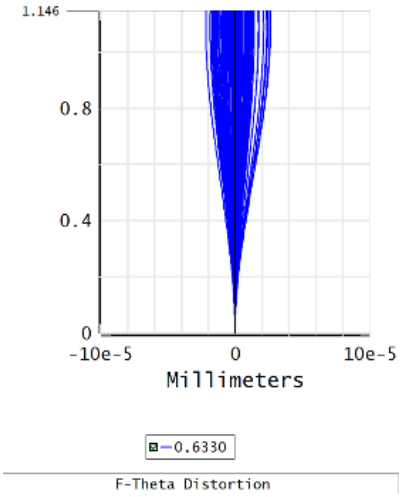

Figure 27. Overlay of all 100 distortion curve for the Monte Carlo tolerance runs. With compensators on the focal distance and image plane tilt, the maximum distortion is on the order of 30nm.

ZOS has a "Zernike Irregularity" surface type that is defined by Zernike polynomial coefficients. It allows for up to 231 terms to be input, terms up to 20th order in radial and azimuthal coordinates. This is useful for importing wavefront measurement data produced by commercial interferometer software into the Lens Editor. But it is also useful in the tolerancing process because the Monte Carlo simulations will automatically compute the coefficients so that they RSS sum to a specified error in terms of height in distance units. Each Monte Carlo realization produces a different set of coefficients. Adding this surface behind the lens and setting the RMS height error to 1nm, we run the Monte Carlo tolerancing simulations and select the best and worst case distortion results. ZOS modifies the parameters in the lens editor file for each realization and saves the specified files as .ZMX files so they can be viewed by themselves to see what the error looks like. When we do this with the 1nm RMS irregularity, we can view the simulated Zernike surface with the Surface Sag Map tool. The worst case realization produces the surface sag map shown in Fig. 28. One can see that it has mainly low frequency features corresponding to the approximately 1.5 mm sampling period of the 20th order polynomial.

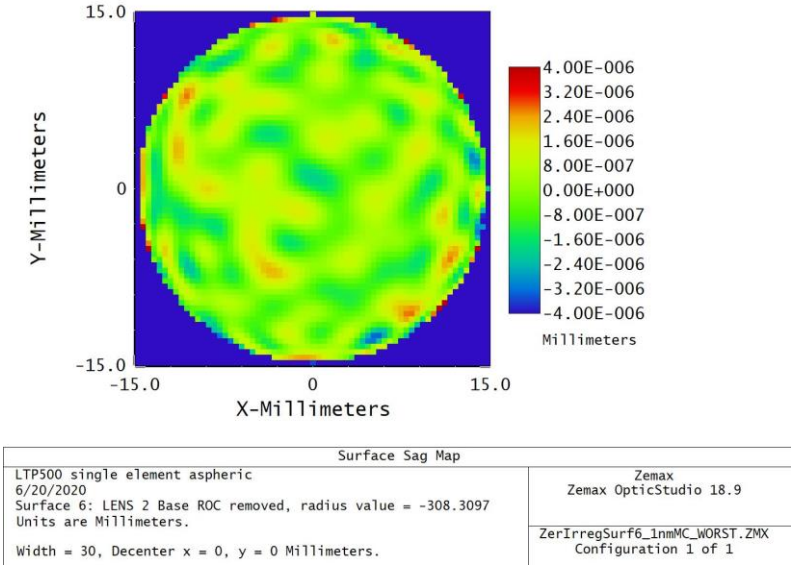

Figure 28. Surface Sag Map for the worst case 1 nm RMS Zernike Irregularity surface produced by the Monte Carlo tolerancing run.

Now we can use the SC model with this Zernike surface to generate POP images as a function of field angle for the laser beam source. This simulates an NSC mode calibration scan. Looking at the residuals in Fig. 29, after fitting the image spots to a Gaussian function, we see that the PV Zernike distortion is less than 0.2 μm with an RMS = 0.060 μm. This error is about an order of magnitude greater than the ideal distortion with no Zernike irregularity, but it is more than two orders of magnitude less than the 60μm PV grid phase surface residual error seen in Fig. 24 and it is one order of magnitude less than the measured Y-slab scan error of 3 μm in Fig. 25 measured by the OMS Y-sab scan. If we consider that the Y-slab scans comprise the collective errors of all 4 surfaces in the doublet lens plus possible glass inhomogeneity, each with a magnitude of 1nm, then scaling the 1nm Zernike result for a single surface by a factor of 5 or so gets the simulation result closer to the measured result. Therefore, we can conclude that the Zernike Irregularity surface gives a better representation of the measured wavefront error than the Grid Phase surface for the current LTP500 lens model.

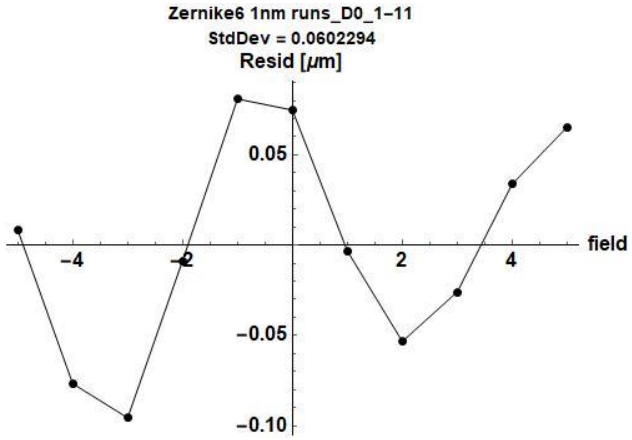

Figure 29.POP image spot Gaussian fit center residuals from worst case 1 nm Zernike irregularity surface.

6. CONCLUSIONS

The use of modern optical design software has allowed us to uncover several sources of error in the original LTP-II system design. Raytracing and physical optics calculation of diffraction images have shown the importance of ghost rays in producing distorted images, compromising the measurements of ultra-precise x-ray mirror surfaces. Deliberate misalignment of the beamsplitter components is necessary to move the ghost images away from the main image spots. However, with the LTP-II design, counter-rotating the BS and PBS to center the SUT beam leaves the REF beam exiting the PBS at a large angle. Several solutions to recovering the reference beam are possible, including adding extra folding mirrors and a separate detector, tilting the entire optical head to make the REF beam collinear with the translation stage axis, or adding a separate autocollimator to measure tilt of the optical head as the carriage moves is translated across the mirror surface. The most recent LTP500 optical head design simplifies the system significantly, eliminating unnecessary glass components and providing for a useful REF beam. Ghost rays are reduced by a small angle twist of the PBS about the Z-axis that also separates the REF and SUT images on the detector. They are further reduced by applying high-performance anti-reflection coatings to the glass surfaces. Wavefront measurements of the cemented doublet designed for the LTP500 that are imported into the ZOS software indicate that improvement in the lens quality is required to enable the system to approach its theoretical performance limits. Addition of an aspheric surface to the lens results in a simplified singlet design with performance superior to the cemented doublet.

7. APPENDIX

7.1. Definition of ZOS "Gaussian" function

The canonical Gaussian probability density function (PDF) of mathematical statistics puts the factor of 2 in the denominator:

$$I_{pdf} \propto e^{-\frac{x^2}{2w^2}} \tag{3}$$

ZOS uses a definition for a "Gaussian" function that differs from the canonical form of the Gaussian probability distribution function. ZOS uses the form where the factor of 2 is in the numerator of the exponent:

$$I_{zemax} \propto e^{-\frac{2x^2}{w^2}} \tag{4}$$

These different forms give different interpretations to the "width" parameter in terms of the $1/e^2$ points on the curve. The radial distance from the center of the spot to the $1/e^2$ point we define as the "base radius". For the ZOS form above, the w-parameter is equal to the base radius, while for the canonical Gaussian PDF, the base radius is twice the w-value. One can see how easily confusion can arise when comparing numerical values of intensity distributions described by different forms of the "Gaussian". We will avoid the term "width" in specifying beam and image properties.

ACKNOWLEDGEMENTS

This work was performed in the scope of subcontracts Nos. 7446674 and 7528983 between The Regents of the University of California and Surface Metrology Solutions LLC,. Research at the Advanced Light Source at Lawrence Berkeley National Laboratory are DOE Office of Science User Facilities under contract no. DE-AC02-05CH11231.

REFERENCES

[1] Zemax *OpticStudio®*, Zemax, LLC, 10230 NE Points Drive, Suite 500, Kirkland, Washington 98033, <zemax.com>

[2] P. Z. Takacs, S. Qian, and J. Colbert, "Design of a Long-Trace Surface Profiler", in *Metrology - Figure and Finish*, Proc. SPIE **749,** pp**.** 59-64 (1987)

[3] P. Z. Takacs, S. K. Feng, E. L. Church *et al.*, "Long trace profile measurements on cylindrical aspheres", in *Advances in Fabrication and Metrology for Optics and Large Optics*, Proc. SPIE **966,** pp**.** 354-364 (1988)

[4] P. Z. Takacs, and S. Qian, "Surface Profiling Interferometer", USA Patent #4,884,697, Dec. 5, 1989

[5] S. C. Irick, W. R. McKinney, D. L. T. Lunt *et al.*, "Using a straightness reference in obtaining more accurate surface profiles," Rev. Sci. Instrum. 63, 1436-1438.

[6] R. D. Geckeler, and I. Weingaertner, "Sub-nm topography measurement by deflectometry: flatness standard and wafer nanotopography", in *Advanced Characterization Techniques for Optical, Semiconductor, and Data Storage Components*, Proc. SPIE **4779,** pp**.** 1-12 (2002)

[7] R. D. Geckeler, A. Just, M. Krause *et al.*, "Autocollimators for deflectometry: Current status and future progress," Nuclear Instruments and Methods in Physics Research Section A: Accelerators, Spectrometers, Detectors and Associated Equipment, 616(2-3), 140-146 (2010).

[8] K. von Bieren, "Pencil Beam Interferometer for Aspherical Optical Surfaces", in *Laser Diagnostics*, Proc. SPIE **343,** pp**.** 101-108 (1982)
[9] K. von Bieren, "Interferometry of Wavefronts Reflected Off Conical Surfaces," Appl. Opt., 22, 2109-2114 (1983).
[10] Advanced Light Source Upgrade (ALS-U) at Lawrence Berkeley Lab; https://als.lbl.gov/als-u/.
[11] S. C. Irick, W. R. McKinney, D. L. Lunt *et al.*, "Using a straightness reference in obtaining more accurate surface profiles from a long trace profiler for synchrotron optics," Review of Scientific Instruments, 63(1), 1436-1438 (1992).
[12] S. C. Irick, "Improved measurement accuracy in a long trace profiler: compensation for laser pointing instability," Nuclear Instruments & Methods in Physics Research, Section A (Accelerators, Spectrometers, Detectors and Associated Equipment), 347(1-3), 226-230 (1994).
[13] S. N. Qian, W. Jark, and P. Z. Takacs, "The Penta-Prism Ltp - a Long-Trace-Profiler with Stationary Optical Head and Moving Penta Prism," Review of Scientific Instruments, 66(3), 2562-2569 (1995).
[14] H. Li, X. Li, M. W. Grindel *et al.*, "Measurement of X-ray Telescope Mirrors Using A Vertical Scanning Long Trace Profiler," Opt. Eng., 35(2), 330-338 (1996).
[15] S. N. Qian, P. Takacs, G. Sostero *et al.*, "Portable long trace profiler: Concept and solution," Review of Scientific Instruments, 72(8), 3198-3204 (2001).
[16] Y. Zhao, Z. Li, D. Li *et al.*, "Principle of π-phase plate long trace profiler for synchrotron radiation optics," Optics Communications, 200(15 Dec 2001), 23-26 (2001).
[17] S. Moriyasu, P. Z. Takacs, J.-i. Kato *et al.*, "On-machine Measurement with the LTP (Long Trace Profiler)", in *Optical Manufacturing and Testing V*, Proc. SPIE **5180,** pp**.** 385-392 (2003)
[18] P. Z. Takacs, and S. Qian, "Sub-microradian error sources in pencil beam interferometry", in *Optical Manufacturing and Testing V*, Proc. SPIE **5180,** pp**.** 377-384 (2003)
[19] S. Qian, Q. Wang, Y. Hong *et al.*, "Multiple functions Long Trace Profiler (LTP-MF) for National Synchrotron Radiation Laboratory of China", in *Advances in Metrology for X-Ray and EUV Optics*, Proc. SPIE **592104,** pp**.** 1-7 (2005)
[20] S. M. Nikitin, G. S. Gevorkyan, W. R. McKinney *et al.*, "New twist in the optical schematic of surface slope measuring long trace profiler", in *Advances in Metrology for X-Ray and EUV Optics VII*, Proc. SPIE **10385,** pp**.** 103850I-1-17 (2017) 10.1117/12.2274400
[21] V. V. Yashchuk, I. Lacey, T. Arnold *et al.*, "Investigation on lateral resolution of surface slope profilers", Proc. SPIE **11109,** pp**.** 111090M/1-19 (2019) doi: 10.1117/12.2539527
[22] I. Lacey, K. Anderson, G. P. Centers *et al.*, "The ALS OSMS: Optical Surface Measuring System for high accuracy two-dimensional slope metrology with state-of-the-art x-ray mirrors", in *Advances in X-Ray/EUV Optics and Components XIII*, Proc. SPIE **10760,** (2018) 10.1117/12.2321347